

Closing the Dequantization Gap: PixelCNN as a Single-Layer Flow

Didrik Nielsen¹ Ole Winther^{1,2}

Abstract

Flow models have recently made great progress at modeling quantized sensor data such as images and audio. Due to the continuous nature of flow models, dequantization is typically applied when using them for such quantized data. In this paper, we propose *subset flows*, a class of flows which can tractably transform subsets of the input space in one pass. As a result, they can be applied directly to quantized data without the need for dequantization. Based on this class of flows, we present a novel interpretation of several existing autoregressive models, including WaveNet and PixelCNN, as single-layer flow models defined through an invertible transformation between uniform noise and data samples. This interpretation suggests that these existing models, 1) admit a latent representation of data and 2) can be stacked in multiple flow layers. We demonstrate this by exploring the latent space of a PixelCNN and by stacking PixelCNNs in multiple flow layers.

1. Introduction

Learning generative models of high-dimensional data poses a significant challenge. The model will have to capture not only the marginal distributions of each of the variables, but also the potentially combinatorial number of interactions between them. Many types of high-dimensional data, with the notable exception of text, are *sensor data* that are generated from some form of physical sensor. Audio, images and video are examples of such data recorded using cameras and microphones. More generally, signals can be recorded using e.g. X-ray scanners, MRI scanners, ultrasonic devices, accelerometers, seismometers, thermometers, chemical sensors etc. Understanding and modeling such data is vital in

¹Department of Applied Mathematics and Computer Science, Technical University of Denmark, Copenhagen, Denmark

²Bioinformatics Centre, Department of Biology, University of Copenhagen, Copenhagen, Denmark. Correspondence to: Didrik Nielsen <didni@dtu.dk>.

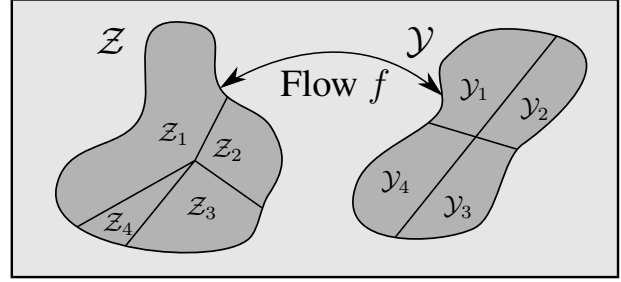


Figure 1: Subset flows $f : Y \rightarrow Z$ allow not only to transform points $z = f(y)$, but also subsets $Z_i = f(Y_i)$, in one pass. As a result, these flows can be trained on quantized data without the need for dequantization.

several branches of science, engineering and medicine.

Deep generative models provide tools for learning the typically high-dimensional, rich structure found in sensor data, utilizing the often vast amounts of unlabeled data available. Generative adversarial networks (GANs) (Goodfellow et al., 2014) is one class of deep generative models that have demonstrated an impressive ability to generate novel plausible-looking images. However, GANs typically lack support over the full data distribution and provide no quantitative measure of performance. *Likelihood-based deep generative models*, on the other hand, do provide this and can be categorized as follows:

1. **Latent variable models** such as Deep Belief Networks (Hinton et al., 2006; Hinton, 2007), Deep Boltzmann Machines (Salakhutdinov & Hinton, 2009), Variational Autoencoders (VAEs) (Kingma & Welling, 2014; Rezende et al., 2014).
2. **Autoregressive models** such as Recurrent Neural Networks (RNNs), MADE (Germain et al., 2015), WaveNet (van den Oord et al., 2016a), PixelCNN (van den Oord et al., 2016c), PixelCNN++ (Salimans et al., 2017), Sparse Transformers (Child et al., 2019).
3. **Flow models** such as RealNVP (Dinh et al., 2017), Glow (Kingma & Dhariwal, 2018), MAF (Papamakarios et al., 2017), FFIORD (Grathwohl et al., 2019).

Sensor data like images and audio arise from physical sensors where continuous signals are converted into digital representations. Through *quantization*, continuous signals are converted into a finite set of discrete values such as $\{0, 1, 2, \dots, 255\}$. The resulting ordinal discrete data is referred to as *quantized data*. Autoregressive models excel at modeling such quantized data as they can directly model discrete distributions. Flow models, on the other hand, are naturally continuous and therefore require *dequantization*, which leads to a lower bound on the discrete likelihood (Theis et al., 2016; Ho et al., 2019).

In this paper:

- We propose subset flows, a class of flows that can be used to train continuous flow-based models directly for quantized data such as images, audio and video without the need for dequantization.
- We show that many existing autoregressive models for quantized data, including WaveNet (van den Oord et al., 2016a), PixelCNN (van den Oord et al., 2016c) and PixelCNN++ (Salimans et al., 2017), can be interpreted as single-layer flows. This gives existing models a notion of a latent space which we demonstrate by exploring the latent space of PixelCNN and PixelCNN++.
- We propose to extend the PixelCNN family of models by stacking them in multiple flow layers and by generalizing the elementwise transformations used. We demonstrate that this can be used to gain improvements over the existing single-layer versions.

Our interpretation provides a unifying view of flow models and discrete autoregressive models for quantized data. Consequently, this work suggests multiple directions for further research on improving the performance of probabilistic generative models for quantized sensor data. The code used for experiments is publicly available at https://github.com/didriknielsen/pixelcnn_flow.

2. Dequantization

Our goal is to model D -dimensional quantized data $\mathbf{x} \in \mathcal{X}$, where typically $\mathcal{X} = \{0, 1, 2, \dots, 255\}^D$. In order to apply a continuous model for such data, dequantization is typically employed. Dequantization refers to the process of converting the discrete, quantized data \mathbf{x} to some continuous $\mathbf{y} \in \mathcal{Y} \subseteq \mathbb{R}^D$.

Uniform dequantization refers to the process of converting the discrete $\mathbf{x} \in \{0, 1, 2, \dots, 255\}^D$ to a continuous $\mathbf{y} \in [0, 256]^D$ by simply adding uniform noise, i.e.

$$\mathbf{y} = \mathbf{x} + \mathbf{u} \quad \text{where} \quad \mathbf{u} \sim \prod_{d=1}^D \text{Unif}(u_d | [0, 1]).$$

This ensures that the values fill the continuous space $[0, 256]^D$ and consequently that continuous models will not collapse towards point masses at the discrete points during training. Uniform dequantization was proposed by Uria et al. (2013) with exactly this motivation. Theis et al. (2016) further showed that optimizing a continuous model on uniformly dequantized samples corresponds to maximizing a lower bound on a discrete log-likelihood.

Variational dequantization was introduced by Ho et al. (2019) as a generalization of uniform dequantization based on variational inference. Let $p(\mathbf{y})$ be some flexible continuous model and assume an observation model of the form

$$P(\mathbf{x}|\mathbf{y}) = \mathbb{I}(\mathbf{y} \in \mathcal{B}(\mathbf{x})),$$

where $\mathcal{B}(\mathbf{x})$ is the region in \mathcal{Y} associated with \mathbf{x} , e.g. a hypercube with one corner in \mathbf{x} , i.e. $\{\mathbf{x} + \mathbf{u} | \mathbf{u} \in [0, 1)^D\}$.

As shown by Ho et al. (2019), using a dequantization distribution $q(\mathbf{y}|\mathbf{x})$, one can develop a lower bound on the discrete log-likelihood $\log P(\mathbf{x})$ using Jensen’s inequality,

$$\begin{aligned} \log P(\mathbf{x}) &= \log \int P(\mathbf{x}|\mathbf{y})p(\mathbf{y})d\mathbf{y} \\ &= \log \int_{\mathbf{y} \in \mathcal{B}(\mathbf{x})} p(\mathbf{y})d\mathbf{y} \\ &= \log \int_{\mathbf{y} \in \mathcal{B}(\mathbf{x})} q(\mathbf{y}|\mathbf{x}) \frac{p(\mathbf{y})}{q(\mathbf{y}|\mathbf{x})} d\mathbf{y} \\ &\geq \int_{\mathbf{y} \in \mathcal{B}(\mathbf{x})} q(\mathbf{y}|\mathbf{x}) \log \frac{p(\mathbf{y})}{q(\mathbf{y}|\mathbf{x})} d\mathbf{y}. \end{aligned}$$

This corresponds exactly to the *evidence lower bound* (ELBO) used in variational inference and VAEs, where the dequantization distribution $q(\mathbf{y}|\mathbf{x})$ coincides with the usual variational posterior approximation.

Note that for uniform dequantization,

$$q(\mathbf{y}|\mathbf{x}) = \prod_{d=1}^D \text{Unif}(y_d | x_d, x_d + 1),$$

and the bound simplifies to

$$\log P(\mathbf{x}) \geq \mathbb{E}_{q(\mathbf{y}|\mathbf{x})}[\log p(\mathbf{y})].$$

Training with this lower bound corresponds to the common procedure for training flows on quantized data, i.e. fit the continuous density $p(\mathbf{y})$ to uniformly dequantized samples \mathbf{y} . Ho et al. (2019) proposed to use a more flexible flow-based dequantization distribution $q(\mathbf{y}|\mathbf{x})$ in order to tighten the bound. The bound can further be tightened by using the importance weighted bound (IWBO) of Burda et al. (2016). In Sec. 3 we will show that, under certain conditions, one can train a continuous flow model directly to optimize $\log P(\mathbf{x})$ instead of a lower bound.

Flow models is a class of models which typically require dequantization when applied for quantized data as they naturally define continuous densities. Flows define a probability density $p(\mathbf{y})$ using an invertible transformation f between \mathbf{y} and a latent \mathbf{z} with a base distribution $p(\mathbf{z})$, i.e.

$$\mathbf{y} = f^{-1}(\mathbf{z}) \quad \text{where} \quad \mathbf{z} \sim p(\mathbf{z}),$$

where f is referred to as a (normalizing) flow (Rezende & Mohamed, 2015). The density of \mathbf{y} can be computed as

$$p(\mathbf{y}) = p(\mathbf{z}) \left| \det \frac{\partial \mathbf{z}}{\partial \mathbf{y}} \right| = p(f(\mathbf{y})) \left| \det \frac{\partial f(\mathbf{y})}{\partial \mathbf{y}} \right|.$$

The main challenge in designing flows is to develop flexible transformations f which are invertible and also have cheap-to-compute Jacobian determinants $|\det \frac{\partial f(\mathbf{y})}{\partial \mathbf{y}}|$. Luckily, more expressive flows can be obtained as a composition $f = f_K \circ \dots \circ f_2 \circ f_1$ of simpler flow layers f_1, f_2, \dots, f_K . The computation cost of the forward pass, the inverse pass and the Jacobian determinant for the composition will simply be the sum of costs for the individual flow layers. While this compositional approach to building expressive densities make flow models attractive, they are not readily applicable to quantized data. Although dequantization allows us to circumvent this, it unfortunately leads to a lower bound on the likelihood.

3. Closing the Dequantization Gap

In this section, we first define the *dequantization gap*, the difference between the discrete log-likelihood and its variational lower bound due to dequantization. Next, we introduce *subset flows*, a class of flows for which dequantization is not needed, allowing us to directly optimize the discrete likelihood.

3.1. The Dequantization Gap

Flow models such as RealNVP (Dinh et al., 2017) and Glow (Kingma & Dhariwal, 2018) have achieved remarkable performance for quantized image data while still allowing efficient sampling with impressive sample quality. However, in terms of log-likelihoods, they still lag behind autoregressive models (Ho et al., 2019; Ma et al., 2019). While some of the performance gap might be the result of less expressive models, much of the gap seems to stem from a loose variational bound, as demonstrated by Ho et al. (2019) and Ma et al. (2019). We term the difference between the discrete log-likelihood and its lower bound the *dequantization gap*:

$$\begin{aligned} \text{Deq. Gap} &:= \log P(\mathbf{x}) - \mathbb{E}_{q(\mathbf{y}|\mathbf{x})} \left[\log \frac{p(\mathbf{y})}{q(\mathbf{y}|\mathbf{x})} \right] \\ &= \mathbb{D}_{KL} [q(\mathbf{y}|\mathbf{x}) \| p(\mathbf{y}|\mathbf{x})]. \end{aligned}$$

In the next subsection, we will introduce *subset flows* which allow the discrete likelihood to be computed in closed form.

This completely closes the dequantization gap and allows us to recover existing autoregressive models as flow models.

3.2. Subset Flows

We define *subset flows* as flows $f : \mathcal{Y} \rightarrow \mathcal{Z}$ which can tractably transform subsets of the input space, $\mathcal{Y}_s \subset \mathcal{Y}$, to subsets in the latent space, $\mathcal{Z}_s \subset \mathcal{Z}$, in a single pass. This is illustrated in Figure 1.

For quantized data $\mathbf{x} \in \{0, 1, 2, \dots, 255\}^D$ we define a continuous space $\mathcal{Y} \subseteq \mathbb{R}^D$, e.g. $[0, 256]^D$. Next, we associate a subset $\mathcal{B}(\mathbf{x}) \subset \mathcal{Y}$, such as $\mathcal{B}(\mathbf{x}) = \{\mathbf{x} + \mathbf{u} | \mathbf{u} \in [0, 1)^D\}$, with each possible value of \mathbf{x} . Any point $\mathbf{y} \in \mathcal{B}(\mathbf{x})$ is deterministically mapped to \mathbf{x} , i.e. $P(\mathbf{x}|\mathbf{y}) = \mathbb{I}(\mathbf{y} \in \mathcal{B}(\mathbf{x}))$. Next, let $p(\mathbf{y})$ be defined using a flow $f : \mathcal{Y} \rightarrow \mathcal{Z}$. We can compute the marginal likelihood $P(\mathbf{x})$ using

$$\begin{aligned} P(\mathbf{x}) &= \int P(\mathbf{x}|\mathbf{y})p(\mathbf{y})d\mathbf{y} = \int_{\mathbf{y} \in \mathcal{B}(\mathbf{x})} p(\mathbf{y})d\mathbf{y} \\ &= \int_{\mathbf{z} \in f(\mathcal{B}(\mathbf{x}))} p(\mathbf{z})d\mathbf{z}, \end{aligned}$$

where $f(\mathcal{B}(\mathbf{x}))$ is the image of f applied to $\mathcal{B}(\mathbf{x})$, i.e. $f(\mathcal{B}(\mathbf{x})) = \{f(\mathbf{y}) | \mathbf{y} \in \mathcal{B}(\mathbf{x})\}$.

Without loss of generality, we can define the base distribution to be standard uniform, $p(\mathbf{z}) = \prod_{d=1}^D \text{Unif}(z_d|0, 1)$. This allows us to obtain the simple formula

$$P(\mathbf{x}) = \int_{\mathbf{z} \in f(\mathcal{B}(\mathbf{x}))} d\mathbf{z} = \text{Volume}(f(\mathcal{B}(\mathbf{x}))). \quad (1)$$

Interestingly, in order to compute $\log P(\mathbf{x})$, we do not need to keep track of infinitesimal volume changes with a Jacobian determinant (as with regular flows). Instead, we have to keep track of the finite volume changes of the set $\mathcal{B}(\mathbf{x})$. While Eq. 1 applies to any flow f in principle, the computation is tractable for subset flows. As such, subset flows can be seen to facilitate *exact* marginalization, allowing exact computation of $P(\mathbf{x})$.

Subset Flows in 1D. Consider a univariate flow f and a uniform base distribution $p(z) = \text{Unif}(z|0, 1)$. In this case,

$$\begin{aligned} P(x) &= \int P(x|y)p(y)dy = \int_{y=x}^{x+1} p(y)dy \\ &= \int_{z=f(x)}^{f(x+1)} p(z)dz = f(x+1) - f(x). \end{aligned}$$

Note that in 1D, f corresponds to the *cumulative distribution function* (CDF) of $p(y)$. Thus, any univariate CDF is also a subset flow. However, note that while subset flows are straightforward to construct in 1D, it is more difficult in higher dimensions. We will now give two examples of subset flows in 1D which we will revisit in subsequent sections.

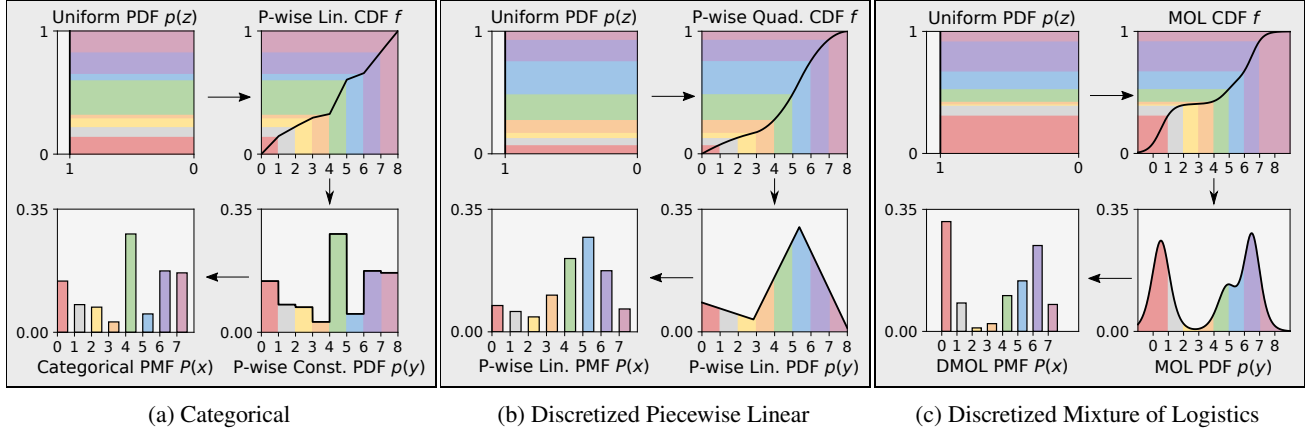


Figure 2: Categorical, Discretized Piecewise Linear and Discretized Mixture of Logistics distributions as 1D subset flows. The *arrows* indicate the direction for **generating samples**: 1) sample uniform noise z , 2) pass z through the inverse flow/CDF f^{-1} to obtain a continuous sample y , 3) quantize y to obtain a discrete sample x . For subset flows, we can tractably invert this process to compute likelihoods. The *colors* illustrate the flow of mass when **computing the likelihood**: 1) determine the region $\mathcal{B}(x)$ associated with observation x , 2) pass the region through the flow (in 1D, pass the two extremes of the region through), 3) compute the volume of the latent region. Note that while subset flows are straightforward in 1D, some care must be taken to extend them to higher dimensions.

The **Categorical** distribution can be obtained using $\mathcal{Y} = [0, K)$ and a piecewise linear CDF f (Müller et al., 2019),

$$f(y) = \sum_{l=1}^{k-1} \pi_l + (y - (k-1))\pi_k$$

for $k-1 \leq y < k$ where $\pi_1, \dots, \pi_K \geq 0$, $\sum_{k=1}^K \pi_k = 1$. This yields a piecewise constant density $p(y)$, which upon quantization yields the Categorical distribution (see Fig. 2a),

$$P(x) = \text{Cat}(x|\pi) = \prod_{k=1}^K \pi_k^{\mathbb{I}(x=k)}.$$

See App. A for details and a quadratic extension (Fig. 2b).

The **Discretized Mixture of Logistics** (DMOL) distribution (Salimans et al., 2017) can be obtained by defining f as the CDF of a mixture of logistics, i.e.

$$f(y) = \sum_{m=1}^M \pi_m \sigma\left(\frac{y - 0.5 - \mu_m}{s_m}\right).$$

With bin boundaries defined at $y \in \{-\infty, 1, 2, \dots, 255, \infty\}$,

$$P(x) = f(y^{\text{upper}}) - f(y^{\text{lower}})$$

$$= \begin{cases} \sum_{m=1}^M \pi_m \left[\sigma\left(\frac{0.5 - \mu_m}{s_m}\right) \right], & x=0 \\ \sum_{m=1}^M \pi_m \left[\sigma\left(\frac{x+0.5 - \mu_m}{s_m}\right) - \sigma\left(\frac{x-0.5 - \mu_m}{s_m}\right) \right], & x=1, \dots, 254 \\ \sum_{m=1}^M \pi_m \left[1 - \sigma\left(\frac{255 - 0.5 - \mu_m}{s_m}\right) \right], & x=255 \end{cases}$$

corresponding exactly to the DMOL distribution as defined in (Salimans et al., 2017). See Fig. 2c for an illustration.

4. PixelCNN as a Single-Layer Flow

In this section, we will first describe autoregressive subset flows, a form of subset flows that are applicable for high-dimensional data. Next, we will show that several existing discrete autoregressive models, including WaveNet, PixelCNN and PixelCNN++, can be obtained as single-layer autoregressive subset flows, giving them a notion of a latent space and enabling extensions such as stacking multiple flow layers.

4.1. Autoregressive Subset Flows

Subset flows present a different set of challenges compared to regular flows. For subset flows, we need not worry about Jacobian determinants. Instead, we need flows where we can keep track of a finite volume. One straightforward approach to do this is to work solely with hyperrectangles. Hyperrectangles have the benefit that they can easily be represented using two extreme points of the hyperrectangle. Furthermore, we can efficiently compute the volume of a hyperrectangle.

In order to work entirely with hyperrectangles, we need two things: 1) we need to partition the continuous space \mathcal{Y} into hyperrectangles $\mathcal{B}(x)$ and 2) we need a flow f such that the regions $f(\mathcal{B}(x))$ resulting from f remain hyperrectangles. The first point is straightforward to achieve. For e.g. $\mathcal{Y} = [0, 256]^D$, we can define $\mathcal{B}(x) = \{x + u | u \in [0, 1)^D\}$, resulting in disjoint hypercubes for each of the discrete values. The second point can be achieved by using an autoregressive flow with *bin conditioning*.

Bin conditioning is achieved by conditioning on the bin to which a value belongs rather than its exact value. For the transformation of dimension d , this is achieved by

$$z_d^{(\text{lower})} = f\left(y_d^{(\text{lower})} | \lambda_d(y_{1:d-1}^{(\text{lower})})\right),$$

$$z_d^{(\text{upper})} = f\left(y_d^{(\text{upper})} | \lambda_d(y_{1:d-1}^{(\text{lower})})\right),$$

where $[y_d^{(\text{upper})}, y_d^{(\text{lower})}]$ are the boundaries of the input hyperrectangle and $[z_d^{(\text{upper})}, z_d^{(\text{lower})}]$ the output hyperrectangle. Importantly, the parameters λ_d are conditioned on the lower corner of the bin, $y_{1:d-1}^{(\text{lower})}$, rather than the exact value $y_{1:d-1}$, thus resulting in the same parameters λ_d regardless of the exact value of $y_{1:d-1}$ within the bin. This is an instance of bin conditioning and ensures that the output region $f(\mathcal{B}(x))$ will remain a hyperrectangle. Fig. 3 illustrates the effect of bin conditioning in a 2-dimensional binary problem. Note that conditioning on the upper corner $y_{1:d-1}^{(\text{upper})}$ or on both corners also are valid choices. Autoregressive subset flows can also be stacked in in multiple layers. See App. C for a discussion on this.

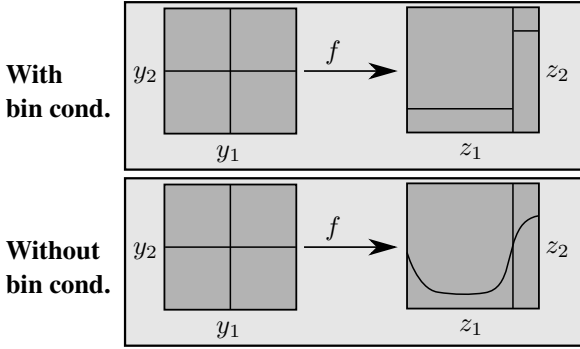


Figure 3: The effect of bin conditioning for a 2-dimensional binary problem. For the transformation with bin conditioning, the transformed rectangles remain rectangles.

4.2. The PixelCNN Family as Flows

Autoregressive models excel at modeling quantized data $x \in \{0, 1, \dots, 255\}^D$ since they can directly model discrete distributions using

$$P(x) = \prod_{d=1}^D P(x_d | x_{1:d-1}).$$

Numerous models of this form have been proposed in recent years (van den Oord et al., 2016c;b;a; Kalchbrenner et al., 2017; Salimans et al., 2017; Parmar et al., 2018; Chen et al., 2018; Menick & Kalchbrenner, 2019; Child et al., 2019). These models rely on autoregressive neural networks constructed using masked convolutions and/or masked self-attention layers and have constituted the state-of-the-art in terms of log-likelihood performance in recent years.

PixelCNN and related models (van den Oord et al., 2016c;b;a; Kalchbrenner et al., 2017; Menick & Kalchbrenner, 2019; Child et al., 2019) rely on the Categorical distribution to model quantized data, i.e.

$$P(x) = \prod_{d=1}^D \text{Cat}(x_d | x_{1:d-1}).$$

As discussed in Sec. 3.2, the Categorical distribution can be obtained by using a piecewise linear transformation, also known as linear splines. Thus, by letting the PixelCNN network parameterize piecewise linear transformations instead of Categorical distributions, one obtains a flow equivalent of PixelCNN. When coupled with a uniform base distribution and applying bin conditioning, the resulting model is a continuous analogue of PixelCNN, which upon quantization corresponds exactly.

PixelCNN can further be extended by replacing the linear splines with higher-order splines such as quadratic, cubic or rational-quadratic splines (Müller et al., 2019; Durkan et al., 2019), yielding novel models. In our experiments, we show that quadratic splines tend to improve performance over linear splines. We refer to this model as PixelCNN (Quad.). The same reasoning can also be applied to the other models related to PixelCNN, such as e.g. WaveNet.

PixelCNN++ and related models (Salimans et al., 2017; Parmar et al., 2018; Chen et al., 2018) use the multivariate discretized mixture of logistics (MultiDMOL) distribution. This is a multivariate generalization of the DMOL presented in Sec. 3.2 and is used to couple the channels for a given spatial location. For an image with $D = CS$ dimension, C channels and S spatial locations,

$$P(x) = \prod_{s=1}^S \text{MultiDMOL}(x_s | x_{1:s-1}),$$

The multivariate DMOL distribution can be obtained as an autoregressive flow using the univariate DMOL flows discussed in Sec. 3.2 as elementwise transformations. See App. B for more details. PixelCNN++ and related models can thus be viewed as *nested autoregressive flows* where the network is autoregressive over the spatial dimensions and outputs parameters for the autoregressive flows along the channels.

5. Related Work

This work is related to several lines of work. First of all, this work builds on work interpreting autoregressive models as flows (Kingma et al., 2016; Papamakarios et al., 2017; Huang et al., 2018; Oliva et al., 2018; Jaini et al., 2019). However, these only apply to continuous distributions and therefore do not include discrete autoregressive models for

quantized data such as the PixelCNN family of models (van den Oord et al., 2016c;b;a; Kalchbrenner et al., 2017; Salimans et al., 2017; Parmar et al., 2018; Chen et al., 2018; Menick & Kalchbrenner, 2019; Child et al., 2019).

Second, this work builds on the variational view of dequantization (Theis et al., 2016; Ho et al., 2019; Hooeboom et al., 2020). Uria et al. (2013) introduced uniform dequantization, Theis et al. (2016) showed that this leads to a lower bound on the discrete likelihood and Ho et al. (2019) further proposed to use a more flexible dequantization distribution in order to tighten the dequantization gap. We expand on this by showing that, for a restricted class of flows, we can perform exact inference and thus close the dequantization gap completely.

Another approach one could take to model discrete data with flows is to make the flows themselves discrete. Hooeboom et al. (2019) present discrete flows for ordinal integer data, while Tran et al. (2019) present discrete flows for nominal categorical data. Both of these works make use of the straight-through estimator (Bengio et al., 2013) to backpropagate through the rounding operations, resulting in a gradient bias. Unlike these works, we make use of with continuous flows, but apply them to discrete data. Consequently, we can compute exact gradients and therefore avoid the performance impacts arising from biased gradients.

6. Experiments

6.1. The Latent Space of PixelCNNs

PixelCNN, PixelCNN++ and related models are typically viewed as purely discrete autoregressive models which have no noise/latent space associated with them. Our interpretation of these models as single-layer flows opens up for exploration of these existing models latent space. To illustrate this possibility, we trained PixelCNN (van den Oord et al., 2016c) and PixelCNN++ (Salimans et al., 2017) as flow models on CIFAR-10. The models obtain 3.14 and 2.92 bits/dim, exactly matching the results of van den Oord et al. (2016c) and Salimans et al. (2017).

We demonstrate that we can interpolate in the latent space to obtain image samples between two existing images. To do this, we first transform two real images $x^{(0)}$ and $x^{(1)}$ to the latent regions $f(\mathcal{B}(x^{(0)}))$ and $f(\mathcal{B}(x^{(1)}))$ and sample according to the uniform base distribution to obtain points $z^{(0)}$ and $z^{(1)}$ in the latent space. Linearly interpolating in this space does not yield uniform samples. Empirically, we found this to often give blurry, single-color interpolations. Instead, we first further transformed the latent images $z^{(0)} \rightarrow h^{(0)}$ and $z^{(1)} \rightarrow h^{(1)}$ using the inverse Gaussian CDF for each dimension. As this is an invertible transformation, we can equivalently consider the base distribution as the isotropic Gaussian. Subsequently, we interpolated

according to

$$h^{(w)} = \frac{w h^{(0)} + (1 - w) h^{(1)}}{\sqrt{w^2 + (1 - w)^2}}, \quad (2)$$

for $0 \leq w \leq 1$. This yields a path of equally probable samples under the base distribution, i.e. $h^{(w)} \sim N(0, 1)$ for $h^{(0)}, h^{(1)} \sim N(0, 1)$. Finally, the intermediate latent points $h^{(w)}$ are transformed back to samples $x^{(w)}$. Some examples of interpolations are shown in Figure 4.



Figure 4: Latent space interpolations between pairs of CIFAR-10 test set images using PixelCNN (odd rows) and PixelCNN++ (even rows). These models are known for capturing local correlations well, but typically struggle with long-range dependencies. This is reflected in several of the interpolated images, which tend to lack global coherence.

6.2. The Effect of the Dequantization Gap

Our work shows that several existing autoregressive models can be viewed as flow models where the dequantization gap between the true likelihood and its variational lower bound is completely closed. We first collect results from existing work in order to compare flow models trained with 1) uniform dequantization, 2) variational dequantization and 3) exact likelihood. The categories should have decreasing dequantization gaps in the listed order. The results are shown in Table 1. We observe significant improvements between the categories, suggesting that the dequantization gap has a significant impact on results.

To further test this hypothesis, we make use of our flow interpretation of existing autoregressive models. We train three flow models on CIFAR-10, 1) PixelCNN, 2) PixelCNN (Quad.) and 3) PixelCNN++ using three different setups:

Table 1: A collection of results from previous work (in bits/dim). We here divide the results into three categories, those trained with: 1) uniform dequantization, 2) variational dequantization and 3) exact likelihood. We observe that performance tends to drastically improve between the categories, suggesting the importance of the dequantization gap for flow models.

Training	Model	CIFAR-10	ImageNet32	ImageNet64
ELBO (Uni.)	RealNVP (Dinh et al., 2017)	3.49	4.28	3.98
	Glow (Kingma & Dhariwal, 2018)	3.35	4.09	3.81
	MaCow (Ma et al., 2019)	3.28	-	3.75
	Flow++ (Ho et al., 2019)	3.29	-	-
ELBO (Var.)	MaCow (Ma et al., 2019)	3.16	-	3.69
	Flow++ (Ho et al., 2019)	3.08	3.86	3.69
Exact	PixelCNN (van den Oord et al., 2016c)	3.14	-	-
	Gated PixelCNN (van den Oord et al., 2016b)	3.03	3.83	3.57
	PixelCNN++ (Salimans et al., 2017)	2.92	-	-
	Image Transformer (Parmar et al., 2018)	2.90	3.77	-
	PixelSNAIL (Chen et al., 2018)	2.85	3.80	3.52
	SPN (Menick & Kalchbrenner, 2019)	-	3.79	3.52
	Sparse Transformer (Child et al., 2019)	2.80	-	3.44

Table 2: The effect of the dequantization gap. We compare three models, PixelCNN, PixelCNN (Quad.) and PixelCNN++. For each model, we trained three versions, one using the exact likelihood and two using the ELBO with uniform dequantization, both with and without bin conditioning. The models trained using the ELBO are evaluated using 1) the ELBO, 2) the IWBO (importance weighted bound) (Burda et al., 2016), and 3) the exact likelihood. See Sec. 6.2 for an explanation.

Bin Cond.	Training	Eval.	PixelCNN	PixelCNN (Q)	PixelCNN++
No	ELBO	ELBO	3.248	3.251	3.112
		IWBO(10)	3.235	3.237	3.095
		IWBO(100)	3.227	3.228	3.086
		IWBO(1000)	3.221	3.223	3.079
Yes	ELBO	ELBO	3.141	3.142	2.993
		IWBO(10)	3.141	3.134	2.983
		IWBO(100)	3.141	3.129	2.978
		IWBO(1000)	3.141	3.126	2.974
		Exact	3.141	3.104	2.944
Yes	Exact	Exact	3.141	3.090	2.924

1. *Exact likelihood:* We train models exploiting the fact that for subset flows we can compute exact likelihoods.
2. *Uniform dequantization w/ bin cond.:* In this case, we train the exact same models as before, but we replace the exact likelihood objective with the ELBO. With this setup, we can investigate:
 - The gap from the ELBO to the exact likelihood: $\log P(\mathbf{x}|\theta_{\text{ELBO}}) - \mathcal{L}(\theta_{\text{ELBO}})$.
 - How much closer the IWBO gets us in practice: $\log P(\mathbf{x}|\theta_{\text{ELBO}}) - \mathcal{L}_k(\theta_{\text{ELBO}})$.
 - The negative impact of training with the ELBO: $\log P(\mathbf{x}|\theta_{\text{Exact}}) - \log P(\mathbf{x}|\theta_{\text{ELBO}})$.

Here, θ denotes the model parameters, $\mathcal{L}(\theta)$ denotes the ELBO and $\mathcal{L}_k(\theta)$ the IWBO with k importance samples for parameters θ . Furthermore, $\theta_{\text{ELBO}} = \arg \max_{\theta} \mathcal{L}(\theta)$ and $\theta_{\text{Exact}} = \arg \max_{\theta} \log P(\mathbf{x}|\theta)$.

3. *Uniform dequantization wo/ bin cond.:* We change the flows to not use bin conditioning. As a result, the latent regions will no longer be hyperrectangles and we can therefore not compute exact likelihoods for these models. Note that this closely corresponds to how most flow models such as RealNVP and Glow are trained.

The results are given in Table 2. Some things to note from these results are:

- The exact models match the reported numbers in van den Oord et al. (2016c) and Salimans et al. (2017) at 3.14 and 2.92 bits/dim.
- Training with the ELBO negatively impacts performance, even when evaluating using the exact likelihood. A small gap of 0.014 and 0.020 bits/dim is found for PixelCNN (Quad.) and PixelCNN++.

- For models with bin conditioning trained with the ELBO, we can here compute the exact dequantization gap. For PixelCNN (Quad.) and PixelCNN++, this gap is found to be 0.038 and 0.049 bits/dim.
- The IWBO improves the estimate of $\log P(\mathbf{x})$ with an increasing number of importance samples. However, even for 1000 samples, less than half the gap has been closed, with 0.022 and 0.030 bits/dim remaining.
- For PixelCNN with bin conditioning, training with the ELBO does not impact performance. Here, the exact $p(\mathbf{y}|\mathbf{x})$ is uniform and therefore exactly matches the uniform dequantization distribution $q(\mathbf{y}|\mathbf{x})$, resulting in a dequantization gap of $\mathbb{D}_{KL}[q(\mathbf{y}|\mathbf{x})||p(\mathbf{y}|\mathbf{x})] = 0$.
- Models trained without bin conditioning show significantly worse performance with gaps of 0.107, 0.161 and 0.188 to the original exact models. This shows that the usual approach of training flows using uniform dequantization and no bin conditioning leads to significantly worse performance.

6.3. Multilayer Subset Flows

We have shown that PixelCNN can be interpreted as a single-layer flow. We now demonstrate that stacking multiple layers of PixelCNN can increase expressiveness. Due to its relative lightweight nature compared to more recent autoregressive models, we use the original architecture of [van den Oord et al. \(2016c\)](#). We train 1, 2 and 4 layers of PixelCNN parameterizing either linear or quadratic splines on CIFAR-10. The results can be found in Table 3. See Fig. 5 for a visualization of how each layer in a multilayer PixelCNN model gradually transform CIFAR-10 test images into noise. See Fig. 6 in App. F for model samples.

The single-layer linear spline case corresponds to the original PixelCNN model and the performance reported here matches [van den Oord et al. \(2016c\)](#) with 3.14 bits/dim. We observe that increasing the number of layers improve the fit over the single-layer version. In fact, the 4-layer version is flexible enough to overfit. By countering this using dropout with a rate of 0.2, the test set performance of the 4-layer version greatly improves, yielding the best performing model. In fact, by simply stacking 4 layers of the original PixelCNN, we outperform the improved model Gated PixelCNN ([van den Oord et al., 2016b](#)). For further performance improvements, models with better inductive biases are needed. However, this is orthogonal to the main focus of this paper and thus left for future work.

In addition to multiple layers improving performance, we observe that quadratic splines improve performance over linear splines in all cases here. For experimental details, see App. D. For PixelCNN++ results, see App. E.1. These are the best reported results for CIFAR-10 among models that

Table 3: Multiple layers of subset flows can be used to obtain more expressive models. We here illustrate this by stacking vanilla PixelCNNs parameterizing either linear or quadratic splines in multiple layers for CIFAR-10. Reported numbers are in bits/dim and training performance in parentheses.

Layers	Dropout	PixelCNN	PixelCNN (Quad.)
1	-	3.14 (3.11)	3.09 (3.05)
2	-	3.07 (2.98)	3.05 (2.96)
4	-	3.09 (2.89)	3.09 (2.88)
	0.2	3.02 (2.98)	3.01 (2.98)



Figure 5: CIFAR-10 test images are transformed to uniform noise (from left-to-right) using $4\times$ PixelCNN (odd rows) and $4\times$ PixelCNN (Quad.) (even rows), both using dropout.

do not use self-attention. Furthermore, we present some results for ImageNet in App. E.2.

7. Conclusion

We presented subset flows, a class of flows which can transform subsets of the input space in a single pass, allowing their use for quantized data like images and audio without the need for dequantization. Through the use of subset flows, one can directly optimize the discrete likelihood and thus completely close the dequantization gap.

Next, we presented autoregressive subset flows, an instance of subset flows that scale to high dimensions. We further showed that existing models such as PixelCNN and WaveNet can be obtained as single-layer autoregressive subset flows. Based on this, we explored the latent space of PixelCNN models and demonstrated performance improvements from stacking multiple flow layers of PixelCNN.

Some interesting directions for future work include designing novel forms of subset flows, exploring the use of subset flows in variational inference, combining subset flows with non-subset flows in hybrid models and building on subset flows to design novel state-of-the-art model architectures.

Acknowledgements

We thank the NVIDIA Corporation for the donation of Titan X GPUs. We thank Emiel Hooeboom, Priyank Jaini, Shihan Wang and Sindy Lwe for helpful feedback.

References

- Bengio, Y., Léonard, N., and Courville, A. C. Estimating or propagating gradients through stochastic neurons for conditional computation. *CoRR*, abs/1308.3432, 2013.
- Burda, Y., Grosse, R. B., and Salakhutdinov, R. Importance weighted autoencoders. In *4th International Conference on Learning Representations, ICLR 2016, San Juan, Puerto Rico, May 2-4, 2016, Conference Track Proceedings*, 2016.
- Chen, X., Mishra, N., Rohaninejad, M., and Abbeel, P. Pixelsnail: An improved autoregressive generative model. In *Proceedings of the 35th International Conference on Machine Learning, ICML 2018, Stockholmsmässan, Stockholm, Sweden, July 10-15, 2018*, pp. 863–871, 2018.
- Child, R., Gray, S., Radford, A., and Sutskever, I. Generating long sequences with sparse transformers. *CoRR*, abs/1904.10509, 2019.
- Dinh, L., Sohl-Dickstein, J., and Bengio, S. Density estimation using real NVP. In *5th International Conference on Learning Representations, ICLR 2017, Toulon, France, April 24-26, 2017, Conference Track Proceedings*, 2017.
- Durkan, C., Bekasov, A., Murray, I., and Papamakarios, G. Neural spline flows. In *Advances in Neural Information Processing Systems 32: Annual Conference on Neural Information Processing Systems 2019, NeurIPS 2019, 8-14 December 2019, Vancouver, BC, Canada*, pp. 7509–7520, 2019.
- Germain, M., Gregor, K., Murray, I., and Larochelle, H. Made: Masked autoencoder for distribution estimation. In *Proceedings of the 32nd International Conference on Machine Learning*, volume 37 of *Proceedings of Machine Learning Research*, pp. 881–889, Lille, France, 07–09 Jul 2015. PMLR.
- Goodfellow, I., Pouget-Abadie, J., Mirza, M., Xu, B., Warde-Farley, D., Ozair, S., Courville, A., and Bengio, Y. Generative adversarial nets. In *Advances in Neural Information Processing Systems 27*, pp. 2672–2680. Curran Associates, Inc., 2014.
- Grathwohl, W., Chen, R. T. Q., Bettencourt, J., Sutskever, I., and Duvenaud, D. FFJORD: free-form continuous dynamics for scalable reversible generative models. In *7th International Conference on Learning Representations, ICLR 2019, New Orleans, LA, USA, May 6-9, 2019*, 2019.
- Hinton, G. E. Learning multiple layers of representation. *Trends in Cognitive Sciences*, 11:428–434, 2007.
- Hinton, G. E., Osindero, S., and Teh, Y. W. A fast learning algorithm for deep belief nets. *Neural Computation*, 18(7):1527–1554, 2006.
- Ho, J., Chen, X., Srinivas, A., Duan, Y., and Abbeel, P. Flow++: Improving flow-based generative models with variational dequantization and architecture design. In *Proceedings of the 36th International Conference on Machine Learning, ICML 2019, 9-15 June 2019, Long Beach, California, USA*, pp. 2722–2730, 2019.
- Hooeboom, E., Peters, J. W. T., van den Berg, R., and Welling, M. Integer discrete flows and lossless compression. In *Advances in Neural Information Processing Systems 32: Annual Conference on Neural Information Processing Systems 2019, NeurIPS 2019, 8-14 December 2019, Vancouver, BC, Canada*, pp. 12134–12144, 2019.
- Hooeboom, E., Cohen, T. S., and Tomczak, J. M. Learning discrete distributions by dequantization. *CoRR*, abs/2001.11235, 2020.
- Huang, C., Krueger, D., Lacoste, A., and Courville, A. C. Neural autoregressive flows. In *Proceedings of the 35th International Conference on Machine Learning, ICML 2018, Stockholmsmässan, Stockholm, Sweden, July 10-15, 2018*, pp. 2083–2092, 2018.
- Jaini, P., Selby, K. A., and Yu, Y. Sum-of-squares polynomial flow. In *Proceedings of the 36th International Conference on Machine Learning, ICML 2019, 9-15 June 2019, Long Beach, California, USA*, pp. 3009–3018, 2019.
- Kalchbrenner, N., van den Oord, A., Simonyan, K., Danihelka, I., Vinyals, O., Graves, A., and Kavukcuoglu, K. Video pixel networks. In *Proceedings of the 34th International Conference on Machine Learning, ICML 2017, Sydney, NSW, Australia, 6-11 August 2017*, pp. 1771–1779, 2017.
- Kingma, D. P. and Ba, J. Adam: A method for stochastic optimization. In *3rd International Conference on Learning Representations, ICLR 2015, San Diego, CA, USA, May 7-9, 2015, Conference Track Proceedings*, 2015.
- Kingma, D. P. and Dhariwal, P. Glow: Generative flow with invertible 1x1 convolutions. In *Advances in Neural Information Processing Systems 31: Annual Conference on Neural Information Processing Systems 2018, NeurIPS 2018, 3-8 December 2018, Montréal, Canada*, pp. 10236–10245, 2018.

- Kingma, D. P. and Welling, M. Auto-encoding variational bayes. In *2nd International Conference on Learning Representations, ICLR 2014, Banff, AB, Canada, April 14-16, 2014, Conference Track Proceedings*, 2014.
- Kingma, D. P., Salimans, T., Józefowicz, R., Chen, X., Sutskever, I., and Welling, M. Improving variational autoencoders with inverse autoregressive flow. In *Advances in Neural Information Processing Systems 29: Annual Conference on Neural Information Processing Systems 2016, December 5-10, 2016, Barcelona, Spain*, pp. 4736–4744, 2016.
- Ma, X., Kong, X., Zhang, S., and Hovy, E. H. Macow: Masked convolutional generative flow. In *Advances in Neural Information Processing Systems 32: Annual Conference on Neural Information Processing Systems 2019, NeurIPS 2019, 8-14 December 2019, Vancouver, BC, Canada*, pp. 5891–5900, 2019.
- Menick, J. and Kalchbrenner, N. Generating high fidelity images with subscale pixel networks and multidimensional upscaling. In *7th International Conference on Learning Representations, ICLR 2019, New Orleans, LA, USA, May 6-9, 2019*, 2019.
- Müller, T., McWilliams, B., Rousselle, F., Gross, M., and Novák, J. Neural importance sampling. *ACM Trans. Graph.*, 38(5):145:1–145:19, 2019.
- Oliva, J. B., Dubey, A., Zaheer, M., Póczos, B., Salakhutdinov, R., Xing, E. P., and Schneider, J. Transformation autoregressive networks. In *Proceedings of the 35th International Conference on Machine Learning, ICML 2018, Stockholmsmässan, Stockholm, Sweden, July 10-15, 2018*, pp. 3895–3904, 2018.
- Papamakarios, G., Murray, I., and Pavlakou, T. Masked autoregressive flow for density estimation. In *Advances in Neural Information Processing Systems 30: Annual Conference on Neural Information Processing Systems 2017, 4-9 December 2017, Long Beach, CA, USA*, pp. 2338–2347, 2017.
- Parmar, N., Vaswani, A., Uszkoreit, J., Kaiser, L., Shazeer, N., Ku, A., and Tran, D. Image transformer. In *Proceedings of the 35th International Conference on Machine Learning, ICML 2018, Stockholmsmässan, Stockholm, Sweden, July 10-15, 2018*, pp. 4052–4061, 2018.
- Rezende, D. J. and Mohamed, S. Variational inference with normalizing flows. In *Proceedings of the 32nd International Conference on Machine Learning, ICML 2015, Lille, France, 6-11 July 2015*, pp. 1530–1538, 2015.
- Rezende, D. J., Mohamed, S., and Wierstra, D. Stochastic backpropagation and approximate inference in deep generative models. In *Proceedings of the 31th International Conference on Machine Learning, ICML 2014, Beijing, China, 21-26 June 2014*, pp. 1278–1286, 2014.
- Salakhutdinov, R. and Hinton, G. Deep boltzmann machines. In *Proceedings of the Twelfth International Conference on Artificial Intelligence and Statistics*, volume 5 of *Proceedings of Machine Learning Research*, pp. 448–455, Hilton Clearwater Beach Resort, Clearwater Beach, Florida USA, 16–18 Apr 2009. PMLR.
- Salimans, T., Karpathy, A., Chen, X., and Kingma, D. P. Pixelcnn++: Improving the pixelcnn with discretized logistic mixture likelihood and other modifications. In *5th International Conference on Learning Representations, ICLR 2017, Toulon, France, April 24-26, 2017, Conference Track Proceedings*, 2017.
- Theis, L., van den Oord, A., and Bethge, M. A note on the evaluation of generative models. In *International Conference on Learning Representations*, Apr 2016.
- Tran, D., Vafa, K., Agrawal, K. K., Dinh, L., and Poole, B. Discrete flows: Invertible generative models of discrete data. In *Advances in Neural Information Processing Systems 32: Annual Conference on Neural Information Processing Systems 2019, NeurIPS 2019, 8-14 December 2019, Vancouver, BC, Canada*, pp. 14692–14701, 2019.
- Uria, B., Murray, I., and Larochelle, H. Rnade: The real-valued neural autoregressive density-estimator. In *Proceedings of the 26th International Conference on Neural Information Processing Systems - Volume 2, NIPS’13*, pp. 2175–2183, USA, 2013. Curran Associates Inc.
- van den Oord, A., Dieleman, S., Zen, H., Simonyan, K., Vinyals, O., Graves, A., Kalchbrenner, N., Senior, A. W., and Kavukcuoglu, K. Wavenet: A generative model for raw audio. *CoRR*, abs/1609.03499, 2016a.
- van den Oord, A., Kalchbrenner, N., Espeholt, L., Kavukcuoglu, K., Vinyals, O., and Graves, A. Conditional image generation with pixelcnn decoders. In *Advances in Neural Information Processing Systems 29: Annual Conference on Neural Information Processing Systems 2016, December 5-10, 2016, Barcelona, Spain*, pp. 4790–4798, 2016b.
- van den Oord, A., Kalchbrenner, N., and Kavukcuoglu, K. Pixel recurrent neural networks. In *Proceedings of the 33rd International Conference on Machine Learning, ICML 2016, New York City, NY, USA, June 19-24, 2016*, pp. 1747–1756, 2016c.

A. Linear and Quadratic Splines as Flows

For self-containedness, we will here summarize linear and quadratic spline flows, i.e. piecewise linear and quadratic flows, as presented by Müller et al. (2019). The linear splines correspond to those presented in Sec. 3.2, but we here provide a more detailed description.

A.1. Linear Spline Flows

Consider a univariate flow $f : \mathcal{Y} \rightarrow \mathcal{Z}$ where $\mathcal{Y} = [0, Q]$ and the latent space $\mathcal{Z} = [0, 1]$. The transformation f is piece-wise linear between the points $\{(y_k, z_k)\}_{k=0}^K$, where

$$0 \equiv y_0 < y_1 < y_2 < \dots < y_K \equiv Q \quad (3)$$

$$0 \equiv z_0 < z_1 < z_2 < \dots < z_K \equiv 1. \quad (4)$$

For piece-wise linear flows, we fix y_1, y_2, \dots, y_{K-1} and parameterize z_1, z_2, \dots, z_{K-1} using probabilities $\pi_1, \pi_2, \dots, \pi_{K-1}$,

$$z_k = \sum_{l=1}^k \pi_l, \quad (5)$$

where $\sum_{l=1}^K \pi_l = 1$.

The forward, inverse and Jacobian determinant computation of a linear spline f can be written as

$$\text{Forward : } z = f(y) = \sum_{k=1}^K \mathbb{I}(y_{k-1} \leq y < y_k) \left[z_{k-1} + \pi_k \frac{y - y_{k-1}}{y_k - y_{k-1}} \right] \quad (6)$$

$$\text{Inverse : } y = f^{-1}(z) = \sum_{k=1}^K \mathbb{I}(z_{k-1} \leq z < z_k) \left[y_{k-1} + (y - y_{k-1}) \frac{z - z_{k-1}}{\pi_k} \right] \quad (7)$$

$$\text{Jac.det. : } \left| \det \frac{df(y)}{dy} \right| = \prod_{k=1}^K \pi_k^{\mathbb{I}(y \in [y_{k-1}, y_k))}. \quad (8)$$

A.1.1. RELATION TO THE CATEGORICAL DISTRIBUTION

To obtain the Categorical distribution, we 1) let $Q = K$, 2) fix $y_0 = 0, y_1 = 1, \dots, y_K = K$ and 3) use a uniform base distribution,

$$z \sim \text{Unif}(z|0, 1) \quad (9)$$

$$y = f^{-1}(z|\pi). \quad (10)$$

This yields a piecewise constant density,

$$p(y|\pi) = \prod_{k=1}^K \pi_k^{\mathbb{I}(y \in [k-1, k))}, \quad (11)$$

which upon quantization yields the Categorical distribution,

$$p(x|\pi) = \text{Cat}(x|\pi) = \prod_{k=1}^K \pi_k^{\mathbb{I}(x=k)}. \quad (12)$$

A.2. Quadratic Spline Flows

Consider again a univariate flow $f : \mathcal{Y} \rightarrow \mathcal{Z}$ where $\mathcal{Y} = [0, Q]$ and the latent space $\mathcal{Z} = [0, 1]$. The transformation f is piece-wise quadratic between the points $\{(y_k, z_k)\}_{k=0}^K$, where

$$0 \equiv y_0 < y_1 < y_2 < \dots < y_K \equiv Q \quad (13)$$

$$0 \equiv z_0 < z_1 < z_2 < \dots < z_K \equiv 1. \quad (14)$$

In the linear spline case, we fixed the locations y_0, y_1, \dots, y_K . If this is not done, the optimization problem would become discontinuous and thus difficult to learn with gradient-based optimizers. In the quadratic case, however, we may let the bin locations y_0, y_1, \dots, y_K be free parameters to be learned (Müller et al., 2019).

The parameters of the flow are given by vectors $\hat{\mathbf{w}} \in \mathbb{R}^K$ and $\hat{\mathbf{v}} \in \mathbb{R}^{K+1}$. The bin widths are computed as

$$\mathbf{w} = Q \cdot \text{softmax}(\hat{\mathbf{w}}), \quad (15)$$

while the bin edges are computed as

$$\mathbf{v} = \frac{\exp(\hat{\mathbf{v}})}{\sum_{k=1}^K \frac{\exp(\hat{v}_k) + \exp(\hat{v}_{k+1})}{2} w_k}. \quad (16)$$

The bin locations are given by the sum of bin widths

$$y_k = \sum_{l=1}^k w_l. \quad (17)$$

For a quadratic spline, the density will be piece-wise linear. We can use this to compute the mass in bin k between the lower extreme y_{k-1} and some point y^* can be computed as

$$\int_{y=y_{k-1}}^{y^*} \left[v_{k-1} + \frac{y - y_{k-1}}{y_k - y_{k-1}} (v_k - v_{k-1}) \right] dy = \int_{t=0}^{\alpha} [v_{k-1} + t(v_k - v_{k-1})] (y_k - y_{k-1}) dt \quad (18)$$

$$= \left[t v_{k-1} + \frac{1}{2} t^2 (v_k - v_{k-1}) \right]_{t=0}^{\alpha} (y_k - y_{k-1}) \quad (19)$$

$$= \left[\alpha v_{k-1} + \frac{1}{2} \alpha^2 (v_k - v_{k-1}) \right] w_k. \quad (20)$$

where $t \equiv \frac{y - y_{k-1}}{y_k - y_{k-1}}$ and $\alpha \equiv \frac{y^* - y_{k-1}}{y_k - y_{k-1}}$. The total mass in the bin can be found by setting $y^* = y_k$ or equivalently $\alpha = 1$ to obtain

$$\int_{y=y_{k-1}}^{y_k} \left[v_{k-1} + \frac{y - y_{k-1}}{y_k - y_{k-1}} (v_k - v_{k-1}) \right] dy = \frac{v_{k-1} + v_k}{2} w_k \quad (21)$$

Using this, we find that

$$z_k = \sum_{l=1}^k \frac{v_{l-1} + v_l}{2} w_l \quad (22)$$

The forward, inverse and Jacobian determinant computation of the resulting quadratic spline flow f can be written as

$$\text{Forward : } z = f(y) = \sum_{k=1}^K \mathbb{I}(y_{k-1} \leq y < y_k) \left[z_{k-1} + w_k \left(\alpha_k v_{k-1} + \frac{1}{2} \alpha_k^2 (v_k - v_{k-1}) \right) \right] \quad (23)$$

$$\text{Inverse : } y = f^{-1}(z) = \sum_{k=1}^K \mathbb{I}(z_{k-1} \leq z < z_k) \left[y_{k-1} + w_k \frac{\sqrt{v_{k-1}^2 + 2 \frac{v_k - v_{k-1}}{w_k} (z - z_{k-1})} - v_{k-1}}{v_k - v_{k-1}} \right] \quad (24)$$

$$\text{Jac.det. : } \left| \det \frac{df(y)}{dy} \right| = [v_{k-1} + \alpha_k (v_k - v_{k-1})]^{\mathbb{I}(y \in [y_{k-1}, y_k])}, \quad (25)$$

where

$$\alpha_k = \frac{y - y_{k-1}}{y_k - y_{k-1}}. \quad (26)$$

B. The Multivariate DMOL as a Flow

We will show that the *multivariate discretized mixture of logistics* (multivariate DMOL) distribution can be obtained as an autoregressive flow. First, we describe the distribution as it was presented in Salimans et al. (2017).

B.1. The Multivariate DMOL Distribution

The discretized logistic distribution can be written as

$$P(x) = \text{DLogistic}(x|\mu, s) = \begin{cases} \sigma\left(\frac{0.5-\mu}{s}\right), & x = 0. \\ \sigma\left(\frac{x+0.5-\mu}{s}\right) - \sigma\left(\frac{x-0.5-\mu}{s}\right), & x = 1, \dots, 254. \\ 1 - \sigma\left(\frac{255-0.5-\mu}{s}\right), & x = 255. \end{cases} \quad (27)$$

The univariate DMOL distribution uses this as mixture components,

$$P(x) = \text{DMOL}(x|\boldsymbol{\pi}, \boldsymbol{\mu}, \mathbf{s}) = \sum_{m=1}^M \pi_m \text{DLogistic}(x|\mu_m, s_m). \quad (28)$$

The multivariate DMOL distribution, on the other hand, can be written as

$$P(\mathbf{x}) = \text{MultiDMOL}(\mathbf{x}|\boldsymbol{\pi}, \boldsymbol{\mu}, \mathbf{s}, \mathbf{r}) = \sum_{m=1}^M \pi_m \text{DLogistic}(x_3|\mu_{3,m}(x_1, x_2, \mathbf{r}_m), s_{3,m}) \text{DLogistic}(x_2|\mu_{2,m}(x_1, \mathbf{r}_m), s_{2,m}) \text{DLogistic}(x_1|\mu_{1,m}, s_{1,m}), \quad (29)$$

where

$$\begin{aligned} \mu_{1,m} &= \mu_{1,m} \\ \mu_{2,m}(x_1, \mathbf{r}_m) &= \mu_{2,m} + r_{1,m}x_1 \\ \mu_{3,m}(x_1, x_2, \mathbf{r}_m) &= \mu_{3,m} + r_{2,m}x_1 + r_{3,m}x_2. \end{aligned} \quad (30)$$

B.2. Rewriting the Multivariate DMOL Distribution

We will now show how one can rewrite this distribution in an autoregressive form. Consider the usual 3-dimensional case and write the multivariate DMOL as

$$P(\mathbf{x}) = \sum_{m=1}^M \pi_m P_m(x_3|x_2, x_1) P_m(x_2|x_1) P_m(x_1). \quad (31)$$

We can rewrite this distribution as

$$P(\mathbf{x}) = \sum_{m=1}^M \pi_m P_m(x_3|x_2, x_1) P_m(x_2|x_1) P_m(x_1) \quad (32)$$

$$\begin{aligned} &= \left[\frac{\sum_{m=1}^M \pi_m P_m(x_3|x_2, x_1) P_m(x_2|x_1) P_m(x_1)}{\sum_{m=1}^M \pi_m P_m(x_2|x_1) P_m(x_1)} \right] \\ &\quad \left[\frac{\sum_{m=1}^M \pi_m P_m(x_2|x_1) P_m(x_1)}{\sum_{m=1}^M \pi_m P_m(x_1)} \right] \\ &\quad \left[\sum_{m=1}^M \pi_m P_m(x_1) \right] \end{aligned} \quad (33)$$

$$= \left[\sum_{m=1}^M \pi_{3,m} P_m(x_3|x_2, x_1) \right] \left[\sum_{m=1}^M \pi_{2,m} P_m(x_2|x_1) \right] \left[\sum_{m=1}^M \pi_{1,m} P_m(x_1) \right] \quad (34)$$

where

$$\begin{aligned} \pi_{1,m} &= \pi_m \\ \pi_{2,m} &= \frac{\pi_m P_m(x_1)}{\sum_{m'=1}^M \pi_{m'} P_{m'}(x_1)} \\ \pi_{3,m} &= \frac{\pi_m P_m(x_2|x_1) P_m(x_1)}{\sum_{m'=1}^M \pi_{m'} P_{m'}(x_2|x_1) P_{m'}(x_1)}. \end{aligned} \quad (35)$$

B.3. The Multivariate DMOL Flow

To summarize, we can write the multivariate DMOL as an autoregressive distribution with univariate DMOL conditionals,

$$\begin{aligned} \text{MultiDMOL}(\mathbf{x}|\boldsymbol{\pi}, \boldsymbol{\mu}, \mathbf{s}, \mathbf{r}) = & \text{DMOL}(x_3|\boldsymbol{\pi}(x_2, x_1), \boldsymbol{\mu}(x_2, x_1, \mathbf{r}), \mathbf{s}) \\ & \cdot \text{DMOL}(x_2|\boldsymbol{\pi}(x_1), \boldsymbol{\mu}(x_1, \mathbf{r}), \mathbf{s}) \\ & \cdot \text{DMOL}(x_1|\boldsymbol{\pi}, \boldsymbol{\mu}, \mathbf{s}), \end{aligned} \quad (36)$$

where the means are given by Eq. 30 and the mixture weights by Eq. 35. Thus, we can obtain the multivariate DMOL flow as an autoregressive flow with the univariate DMOL flows from Sec. 3.2 as elementwise transformations.

C. Multilayer Autoregressive Subset Flows

Denote the intermediate spaces as $\mathbf{z}_l, l = 0, 1, \dots, L$ with $\mathbf{y} \equiv \mathbf{z}_0$ and $\mathbf{z} \equiv \mathbf{z}_L$. In a layer l , we further denote the boundaries of the hyperrectangle for dimension d as $z_{d,l}^{(\text{lower})}$ and $z_{d,l}^{(\text{upper})}$. The procedure for computing the likelihood in a multilayer autoregressive subset flow is shown in Algo. 1, while the procedure for sampling is shown in Algo. 2.

Algorithm 1 Likelihood Computation for AR Subset Flows

```

Observe quantized  $\mathbf{x}$ 
Define  $\mathbf{z}_0^{(\text{lower})} = \mathbf{x}, \mathbf{z}_0^{(\text{upper})} = \mathbf{x} + 1$ 
for  $l = 1$  to  $L$  do
    Compute  $\boldsymbol{\lambda}_l \leftarrow \text{AutoregNetwork}(\mathbf{z}_{l-1}^{(\text{lower})})$ .
    Transform  $\mathbf{z}_l^{(\text{lower})} = f_l^{-1}(\mathbf{z}_{l-1}^{(\text{lower})}|\boldsymbol{\lambda}_l)$ .
    Transform  $\mathbf{z}_l^{(\text{upper})} = f_l^{-1}(\mathbf{z}_{l-1}^{(\text{upper})}|\boldsymbol{\lambda}_l)$ .
end for
Compute  $P(\mathbf{x}) = \prod_{d=1}^D [z_{l,d}^{(\text{upper})} - z_{l,d}^{(\text{lower})}]$ .
```

Algorithm 2 Sampling for AR Subset Flows

```

Sample  $\mathbf{z} \sim \prod_{d=1}^D \text{Unif}(z_d|0, 1)$ 
for  $d = 1$  to  $D$  do
    for  $l = 1$  to  $L$  do
        Compute  $\boldsymbol{\lambda}_{l,d} \leftarrow \text{AutoregNetwork}(\mathbf{z}_{l-1,1:d-1}^{(\text{lower})})$ .
        Transform  $z_{l,d} = f_{l,d}^{-1}(z_{l,d}| \boldsymbol{\lambda}_{l,d})$ .
    end for
    Define  $y_d = z_{0,d}$ .
    Quantize  $y_d$  to obtain a quantized sample  $x_d$ .
end for
```

D. Experimental Details

The code used for experiments is publicly available¹. In our experiments, we used PixelCNN (van den Oord et al., 2016c) and PixelCNN++ (Salimans et al., 2017) models. For hyperparameters, we followed the original architectures as closely as possible. The PixelCNN architecture we used for the CIFAR-10 experiments is summarized in Table 4.

Table 4: The PixelCNN architecture used for the CIFAR-10 dataset.

3 x 32 x 32 RGB Image
Conv7x7(256) (Mask A)
15 Residual Blocks, each using:
ReLU - Conv1x1(256) (Mask B)
ReLU - Conv3x3(128) (Mask B)
ReLU - Conv1x1(256) (Mask B)
ReLU - Conv1x1(1024) (Mask B)
ReLU - Conv1x1(#param) (Mask B)

For the PixelCNN++ we used, like Salimans et al. (2017), 6 blocks with 5 ResNet layers. Between blocks 1 and 2 and between blocks 2 and 3, strided convolutions are used to downsample the feature maps. Between blocks 4 and 5 and between blocks 5 and 6, transposed strided convolutions are used to upsample the feature maps back to the original size. Shortcut connections are added from block 1 to 6, 2 to 5 and 3 to 4. For more details on the PixelCNN++ architecture see Salimans et al. (2017) and their publicly available code².

¹https://github.com/didriknielsen/pixelcnn_flow

²<https://github.com/openai/pixel-cnn>

For models using linear splines we used 256 bins, corresponding to the quantization level. For models using quadratic splines, we used 16 bins as this was found to work well in early experiments. Note that for quadratic splines, the bin locations can also be learned (Müller et al., 2019). As a consequence, less bins are typically required than for linear splines. Finally, for models using DMOL, 10 mixtures were used.

All models trained for the CIFAR-10 dataset were trained for 500 epochs with a batch size of 16. The Adam optimizer (Kingma & Ba, 2015) was used. The learning rate was initially $4 \cdot 10^{-3}$ and decayed by 0.5 at epochs 250, 300, 350, 400, 450.

E. Additional Results

E.1. Experiments for PixelCNN++

We here experiment with combining PixelCNN++ (Salimans et al., 2017) with other models in a multilayer flow. We use the original PixelCNN++ architecture and combine this with the original PixelCNN architecture (van den Oord et al., 2016c) parameterizing quadratic splines with 16 bins. We train this combination in both orders. The PixelCNN architecture here uses a dropout rate of 0.5, matching that of the PixelCNN++ architecture. The results are shown in Table 5.

We observe some slight improvements from combining PixelCNN++ with other models. Earlier experiments indicated that improving on PixelCNN++ by combining it with more layers of PixelCNN or PixelCNN++ was difficult since this often resulted in severe overfitting. We thus observe only mild improvements over the original model by combining it with other flows. We note that these are the best reported results for CIFAR-10 among models that only use convolutions and do not rely on self-attention. For further improvements, incorporating self-attention in the model would thus probably be of help.

All models here were trained for 500 epochs with a batch size of 16. The Adam optimizer (Kingma & Ba, 2015) was used. The learning rate was initially $4 \cdot 10^{-3}$ and decayed by 0.5 at epochs 250, 300, 350, 400, 450.

Table 5: PixelCNN++ with combined with PixelCNN (Quad.) for the CIFAR-10 dataset.

Model	Bits/dim
PixelCNN++	2.924
PixelCNN++ & PixelCNN (Quad.)	2.914
PixelCNN (Quad.) & PixelCNN++	2.906

E.2. Experiments for ImageNet 32x32 and 64x64

In addition to training PixelCNN (van den Oord et al., 2016c) models in multiple flow layers for CIFAR-10, we here attempt the same for the 32x32 and 64x64 ImageNet datasets. For simplicity, all parameters were kept the same as in the case of CIFAR-10, except that 20 residual blocks were used for ImageNet64 (due to the need of a larger receptive field). The results for PixelCNN, 2×PixelCNN and 2×PixelCNN (Quad.) are shown in Table 6. We observe that performance improves with 2 layers instead of 1 and that swapping linear splines with quadratic splines further improves performance. Note that the performance of these models are slightly sub-par compared to other results by autoregressive models for these datasets. We attribute this to the fact that most other work use larger models, such as more filters in the convolutional layers, than the simple PixelCNN architectures we used here. Regardless, these results show that stacking more layers also helps for the 32x32 and 64x64 ImageNet datasets.

The ImageNet32 models were trained for 30 epochs with a batch size of 16, while the ImageNet64 models were trained for 20 epochs with a batch size of 8. The Adam optimizer (Kingma & Ba, 2015) was used. The learning rate was initially $4 \cdot 10^{-3}$ and decayed by 0.5 at epochs 15, 18, 21, 24, 27 (for ImageNet32) and epochs 10, 12, 14, 16, 18 (for ImageNet64).

Table 6: Multiple layers of vanilla PixelCNNs for the 32x32 and 64x64 ImageNet datasets. Here, very simple PixelCNN networks are used

Model	ImageNet32	ImageNet64
PixelCNN	3.96	3.67
2 × PixelCNN	3.91	3.63
2 × PixelCNN (Quad.)	3.90	3.61

F. Samples

See Fig. 6 for samples from PixelCNN, PixelCNN (Quad.) and 4-layer version of the same models.

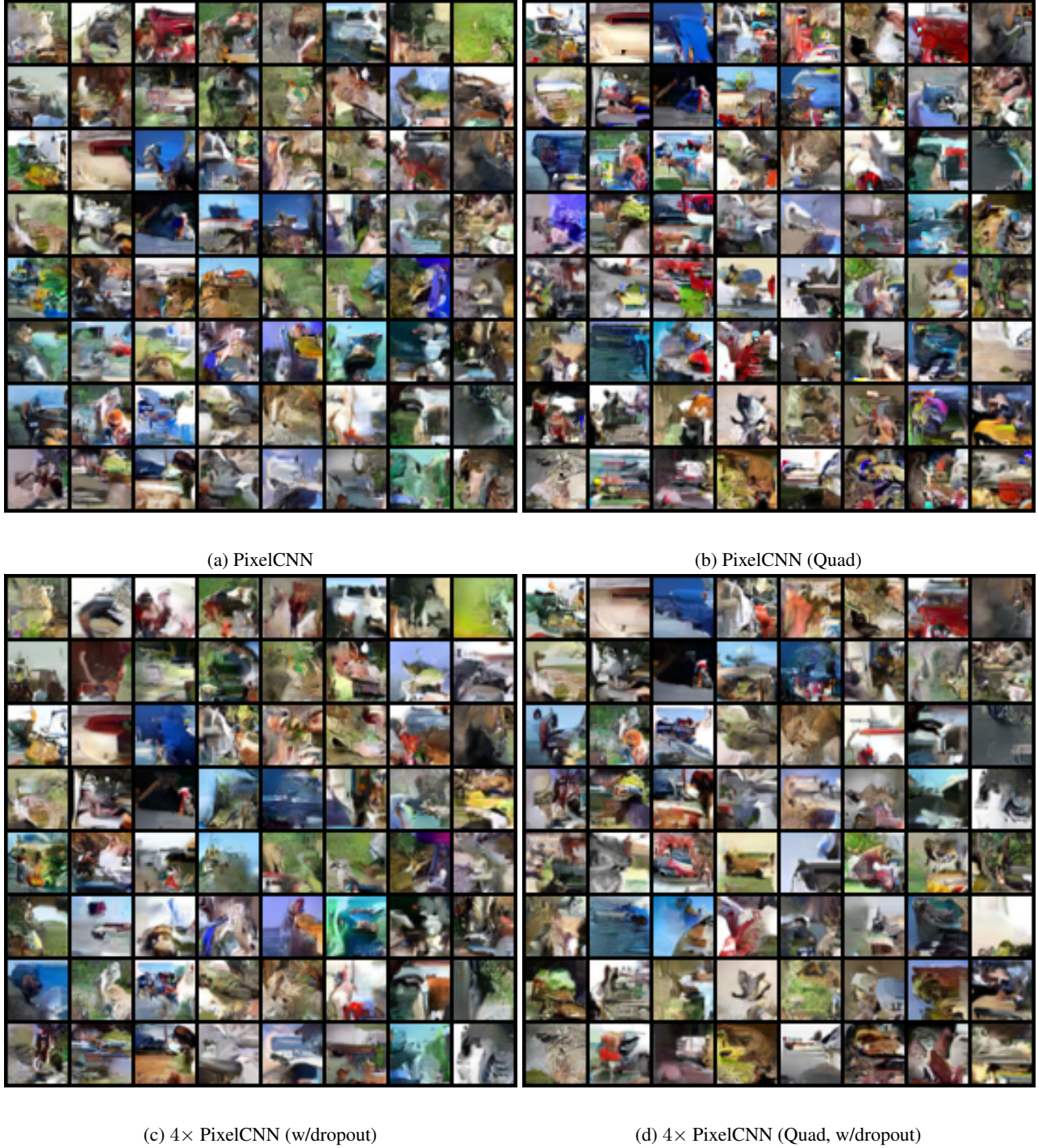


Figure 6: Unconditional samples from PixelCNN-based flow models trained on the CIFAR-10 dataset. The perceptual quality appears similar, or perhaps slightly better, for the multilayer flows. Note that for ease of comparison, the same uniform noise was passed through all models, resulting in a noticeable similarity in the samples across different models.